

PARSEC evolutionary tracks of massive stars up to $350 M_{\odot}$ at metallicities $0.0001 \leq Z \leq 0.04$

Yang Chen,^{1,2★†} Alessandro Bressan,^{2★} Léo Girardi,^{3★} Paola Marigo,⁴ Xu Kong^{1,5} and Antonio Lanza²

¹Department of Astronomy, University of Science and Technology of China (USTC), Hefei 230026, Anhui, China

²SISSA, via Bonomea 265, I-34136 Trieste, Italy

³Osservatorio Astronomico di Padova – INAF, Vicolo dell’Osservatorio 5, I-35122 Padova, Italy

⁴Dipartimento di Fisica e Astronomia, Università di Padova, Vicolo dell’Osservatorio 2, I-35122 Padova, Italy

⁵Key Laboratory for Research in Galaxies and Cosmology, USTC, Chinese Academy of Sciences, Hefei 230026, Anhui, China

Accepted 2015 June 5. Received 2015 June 5; in original form 2015 April 14

ABSTRACT

We complement the PARSEC data base of stellar evolutionary tracks with new models of massive stars, from the pre-main-sequence phase to the central carbon ignition. We consider a broad range of metallicities, $0.0001 \leq Z \leq 0.04$ and initial masses up to $M_{\text{ini}} = 350 M_{\odot}$. The main difference with respect to our previous models of massive stars is the adoption of a recent formalism accounting for the mass-loss enhancement when the ratio of the stellar to the Eddington luminosity, Γ_e , approaches unity. With this new formalism, the models are able to reproduce the Humphreys–Davidson limit observed in the Galactic and Large Magellanic Cloud colour–magnitude diagrams, without an ad hoc mass-loss enhancement. We also follow the predictions of recent wind models indicating that the metallicity dependence of the mass-loss rates becomes shallower when Γ_e approaches unity. We thus find that the more massive stars may suffer from substantial mass-loss even at low metallicity. We also predict that the Humphreys–Davidson limit should become brighter at decreasing metallicity. We supplement the evolutionary tracks with new tables of theoretical bolometric corrections, useful to compare tracks and isochrones with the observations. For this purpose, we homogenize existing stellar atmosphere libraries of hot and cool stars (Potsdam Wolf–Rayet, ATLAS9 and PHOENIX) and we add, where needed, new atmosphere models computed with WM-BASIC. The mass, age and metallicity grids are fully adequate to perform detailed investigations of the properties of very young stellar systems, both in local and distant galaxies. The new tracks supersede the previous old PADOVA models of massive stars.

Key words: stars: evolution – Hertzsprung–Russell and colour–magnitude diagrams – stars: massive – stars: mass-loss – supergiants – stars: Wolf–Rayet.

1 INTRODUCTION

Massive stars play an important role in the evolution of galaxies. They are the most important stellar sources of ionizing and dissociation photons (Hollenbach & Tielens 1999; Schaerer et al. 2011; Dale, Ercolano & Bonnell 2012; Cai et al. 2014; Kimm & Cen 2014; Yu, Wang & Li 2015). They inject a significant amount of kinetic energy through powerful stellar winds (Mackey et al. 2014). They are among the main drivers of metal and dust enrichment in galaxies when they explode as core collapsed supernovae (Schneider, Ferrara & Salvaterra 2004; Sarangi & Cherkneff 2015). They are thus very important sources of feedback to the ambient ISM (Dale, Ercolano

& Bonnell 2013). Last but not least, most of our information on the ongoing star formation rates across the Universe heavily relies on our detailed knowledge of their properties (Kennicutt 1998; Bruzual & Charlot 2003).

Because of their relevance for so many fields of astrophysics, massive stars have been the subject of many observational and theoretical investigations that are impossible to list here. Understanding their evolution is challenged by the complexity of several physical phenomena, as recently reviewed, for example, by Martins & Palacios (2013) who compare STERN (Brott et al. 2011), GENEVA (Ekström et al. 2012), FRANEC (Chieffi & Limongi 2013), PADOVA (Bertelli et al. 2009), MESA (Paxton et al. 2011) and STAREVOL (Decressin et al. 2009) evolutionary tracks of massive stars. Martins & Palacios (2013) find that, apart from the inclusion of rotation, the main differences among the models computed by different authors can be attributed to the different treatments of convection and

*E-mail: ychen@sissa.it (YC); sbressan@sissa.it (AB); leo.girardi@oapd.inaf.it (LG)

† YC is supported by the SISSA-USTC joint doctoral programme.

mass-loss, with the former process being more important in the domain of the less massive stars. It is worth noting that the PADOVA tracks (Bertelli et al. 2009) analysed by Martins & Palacios (2013) are still those presented in Fagotto et al. (1994) and Bressan et al. (1993). Since then, there have been many advances both in the basic input physics (opacities, equation of state, nuclear reactions) and in the mass-loss theory (and observations), and these called for a substantial revision of the PADOVA code. But, while low and intermediate mass stars were systematically updated, with the last version being PARSEC (PADOVA T Rieste Stellar Evolution Code) models (Bressan et al. 2012, and refs. therein), massive stars have not been updated since then.

In this paper, we present the new evolutionary tracks of massive stars computed with PARSEC. Besides the basic input physics, which is described elsewhere (Bressan et al. 2012, and refs. therein), the main novelties concern the recipes adopted for the mass-loss rates and the spectral energy distributions used to convert the tracks from the theoretical to the observational plane. Concerning mass-loss, there have been many efforts over the past years to determine/predict the mass-loss rates of massive stars across different spectral types and metallicities. It is now widely accepted that hot massive blue supergiants (BSGs) and Wolf–Rayet (WR) stars lose a prominent amount of their mass through line-driven stellar winds and that the mass-loss rates show a simple scaling law with the metallicity (Castor, Abbott & Klein 1975; Kudritzki & Puls 2000; Nugis & Lamers 2000; Vink, de Koter & Lamers 2000, 2001; Crowther 2007; Muijres et al. 2012a; Smith 2014). In Luminous Blue Variable (LBV) stars, there is evidence that an important mode of mass-loss is through eruptive mass-loss, that may contribute as much as or even more than the steady stellar wind (Smith 2009). In this phase the mass-loss rate may easily reach a few of $10^{-4} M_{\odot} \text{ yr}^{-1}$ (Lamers 1989). This eruptive mechanism is still unknown but the observed rates could be explained by a super-Eddington wind (Smith & Owocki 2006), or by non-disruptive hydrodynamic explosions (Barsukova et al. 2014). Interestingly, LBV stars are found near the so-called Humphreys–Davidson limit (Humphreys & Davidson 1979) which delimits the forbidden region above which only very few stars are observed in the Hertzsprung–Russell (HR) diagram of the Galactic massive stars. In this respect, a remarkable result of recent investigations is that the mass-loss rates could be enhanced by a significant factor when the stars approach the Eddington luminosity (Gräfener & Hamann 2008; Vink et al. 2011), which is known to happen near the Humphreys & Davidson (1979) limit. For the later spectral types there are larger uncertainties both on the mechanisms and on the strength of the mass-loss rates. In red supergiants (RSG) one customarily adopts the observational parametrization by de Jager, Nieuwenhuijzen & van der Hucht (1988), but the mass-loss rates in this phase are known to be uncertain by a large factor (Salasnich, Bressan & Chiosi 1999; Meynet et al. 2015). As in less massive asymptotic giant branch stars, dust formation on the circumstellar envelopes could be one of the possible mechanisms responsible for this enhancement (van Loon et al. 2005).

Concerning the atmosphere models used to predict the stellar magnitudes and colours, they are equally important for the interpretation of observed properties of massive stars. For stars with negligible mass-loss, a comprehensive stellar atmosphere library usually adopted is ATLAS9 (Castelli & Kurucz 2004), consisting of plane parallel models in local thermodynamic equilibrium (LTE). This library is particularly suitable for \sim A-, F- and G-type stars. For cool giants, where the plane parallel and non-LTE approximations must be relaxed, comprehensive stellar atmosphere libraries are provided by PHOENIX (Allard et al. 2012, and references therein)

and MARCS (Gustafsson et al. 2008) projects. For hot stars with high mass-loss rates a number of atmosphere models have been released in the recent years like the WM-BASIC models (Pauldrach, Puls & Kudritzki 1986), the CMFGEN models (Hillier & Miller 1998) and the Potsdam Wolf–Rayet (POWER) models (Gräfener, Koesterke & Hamann 2002; Hamann & Gräfener 2003, 2004; Sander, Hamann & Todt 2012; Hamann, Gräfener & Liermann 2006; Hainich et al. 2014).

The paper is organized as following. In Section 2, we describe our stellar evolution models for massive stars, with particular care to the description of the recipes adopted for the mass-loss rates. In this section, we also compare the new models with our previous models and with one set among the most recent models found in literature, FRANEC (Chieffi & Limongi 2013). In Section 3, we describe in detail the adopted atmosphere models and the procedure used to obtain as much as possible homogeneous sets of bolometric correction (BC_{λ}) tables. Finally, in Section 4, we discuss the resulting colour–magnitude diagrams predicted from the new evolutionary tracks and isochrones.

Our evolutionary tracks can be downloaded from <http://people.sissa.it/~sbressan/parsec.html>, and the isochrones can be downloaded from <http://stev.oapd.inaf.it/cgi-bin/cmd>.

2 STELLAR EVOLUTIONARY TRACKS

We compute new tracks of massive stars with the PARSEC code for a wide range of initial metallicities and for initial masses from $M_{\text{ini}} = 14 M_{\odot}$ to $M_{\text{ini}} = 350 M_{\odot}$. The evolution begins from the pre-main-sequence phase and ends at central carbon ignition. The new evolutionary tracks complement the already existing models of intermediate and low-mass stars.

2.1 Basic input physics

The input physics used in PARSEC is already thoroughly described in Bressan et al. (2012), Bressan et al. (2013) and Chen et al. (2014). Below we briefly summarize the main points with particular attention to those more relevant to the massive stars. The equation of state (EOS) is computed with the FREEEOS code of A.W. Irwin.¹ Radiative opacities are from the OPAL project (Iglesias & Rogers 1996) and, in the low-temperature regime, from the AESOPUS² project (Marigo & Aringer 2009). Conductive opacities are included following Itoh et al. (2008). The nuclear reaction rates (p–p chains, CNO tri-cycle, Ne–Na and Mg–Al chains and the most important α -capture reactions including the α -n reactions) and the corresponding Q -values are taken from the recommended rates in the JINA reaclib data base (Cyburt et al. 2010). Electron screening factors for all reactions are from Dewitt, Graboske & Cooper (1973) and Graboske et al. (1973). Finally, electron neutrinos energy losses are computed following Munakata, Kohyama & Itoh (1985), Itoh & Kohyama (1983) and Haft, Raffelt & Weiss (1994).

The metal abundances, $0.0001 \leq Z \leq 0.04$, follow the partition of Grevesse & Sauval (1998, hereafter GS98) with the recent revision by Caffau et al. (2011). With this revision, the current observed solar metallicity is $Z_{\odot} = 0.01524$. The initial helium content at varying metallicity is determined by $Y = Y_{\text{p}} + 1.78 \times Z$, with $Y_{\text{p}} = 0.2485$ taken from Komatsu et al. (2011).

¹ <http://freeeos.sourceforge.net>.

² <http://stev.oapd.inaf.it/aesopus>.

2.2 Convection, overshooting and mixing

The mixing length parameter (Böhm-Vitense 1958), derived from the solar model, is $\alpha_{\text{MLT}} = 1.74$. We adopt the Schwarzschild criterion (Schwarzschild 1958) to test the stability of radiative zones against convection. In the presence of a gradient of chemical composition, an alternative criterion is that of Ledoux (Ledoux 1947). This condition may happen during the evolution of massive stars when the convective core grows in mass or when an intermediate radiative region of varying chemical composition becomes unstable to the convection. In this paper, we opt for the Schwarzschild criterion because, on one side it has been shown that it is the more appropriate one to account for the effects of thermal dissipation (Kato 1966) and, on the other, the presence of a sizable overshooting region from the convective core significantly reduces the differences between models computed with the two alternative criteria (Meynet & Maeder 2000).

Overshooting from the convective core is estimated within the framework of the mixing-length theory, allowing for the penetration of convective elements into the stable regions (Bressan, Chiosi & Bertelli 1981). The adopted mean free path of convective elements *across* the border of the unstable region, $l_c = \Lambda_c H_p$ with $\Lambda_c = 0.5$, is calibrated on the colour–magnitude diagram of intermediate age clusters (Girardi, Rubele & Kerber 2009) as well as on individual stars (Deheuvels et al. 2010; Kamath et al. 2010; Torres et al. 2014). We also account for overshooting at the base of the convective envelope, which is simply modelled by mixing the radiative region down to a distance of $l_e = 0.7 H_p$ from the formal Schwarzschild border (Alongi et al. 1991). We stress that the extent of the overshooting regions and the corresponding mixing efficiencies are still a matter of debate. Concerning core overshooting, a recent analysis of the period spacing of gravity modes in low mass helium burning stars, suggests a quite sizable overshooting region, $\Lambda_c = 1.0$ in the above formalism (Bossini et al. 2015, in preparation). Concerning envelope overshooting, work in progress (Tang et al. 2014 and Rosenfield et al., in preparation) already indicates that using larger values of l_e (close to $2 H_p$) at the bottom of the convective envelope fits better the extended blue loops seen in metal-poor dwarf galaxies. Therefore, future releases of the PARSEC data base are likely to have these prescriptions revised.

Finally, rotational mixing has not yet been introduced in PARSEC.

2.3 Mass-loss rates

At solar metallicity, the mass-loss phenomenon is known to dominate the evolution of stars for initial masses $M_{\text{ini}} \geq 30 M_{\odot}$. We account for this process following recent prescriptions found in the literature for the different spectral types. In the BSG phase, for $T_{\text{eff}} \geq 12000$ K, we adopt the relations provided by Vink et al. (2000, 2001). This formulation (R_{V01}) shows an almost linear overall dependence of the mass-loss rates on the metallicity, $\dot{M} \propto (Z/Z_{\odot})^{0.85} M_{\odot} \text{ yr}^{-1}$. In the supergiant phases with $T_{\text{eff}} < 12000$ K we use the mass-loss rates provided by de Jager et al. (1988), R_{dl} , assuming the same dependence on the surface metallicity of R_{V01} . For WR stars we use the Nugis & Lamers (2000) formalism, R_{NL} . They also provide a dependence on the stellar metallicity. The definition of the WR phases is provided below (see Section 3.2).

An aspect which is relevant for the more massive stars concerns the transition between the O-phase, the LBV/RSG phase and finally the WR phase and, most importantly, the dependence

of this transition upon the metallicity of the stars. For example, in the old PADOVA models, e.g. Bressan et al. (1993), the transition to the superwind phase corresponding to the LBV stars is artificially set at the stages when the models cross the Humphreys–Davidson instability limit (Humphreys & Davidson 1979) in the HR diagram. This is justified by the evidence that Galactic and Magellanic Clouds massive stars near this limit show mass-loss rates that may reach $\dot{M} \simeq 10^{-3} M_{\odot} \text{ yr}^{-1}$. However, while the Humphreys–Davidson limit is an observed property of the HR diagram of massive stars in near solar environments, it is used independently from the metallicity of the galaxy, in spite of the fact that the mass-loss rates themselves do depend on the abundance of heavy elements (Kudritzki & Puls 2000; Puls, Springmann & Lennon 2000; Mokieim et al. 2007; Smith 2014). This approximation becomes critical at very low metallicities.

From the theoretical side, recent detailed studies of radiative wind models (Gräfener & Hamann 2008 and Vink et al. 2011) show that the mass-loss rates are strongly enhanced when the stars approach the electron scattering Eddington limit

$$\Gamma_e = \frac{L\kappa_{es}}{4\pi cGM} = 1. \quad (1)$$

Since for the most massive stars at solar metallicity this may happen near the Humphreys–Davidson limit, the above formalisms could provide a modern description of the transition from O-type through LBV/RSG-type to WR-types (Vink & Gräfener 2012). We thus include in PARSEC the recent formulation of mass-loss rates by Vink et al. (2011). The resulting HR diagram of a few selected evolutionary tracks for about solar metallicity is shown in the upper panel of Fig. 1. For purposes of clearness, we do not plot the pre-main-sequence phase. The colours along the tracks represent the strength of the mass-loss rates as indicated in the inset scale. In the figure, the thick black lines mark the so-called Humphreys–Davidson limit (Humphreys & Davidson 1979) which delimit the forbidden region above which only very few stars are observed in the HR diagram of the Galactic massive stars. As shown in the figure, the main sequence of the most massive stars extends up to the Humphreys–Davidson limit. Eventually, the stars may encompass this limit but the time spent in this region is very short because the mass-loss rate becomes so high that the stars rapidly lose their envelopes and turn into the hotter region of the HR diagram. We stress that this is not a result of an ad hoc assumption for the mass-loss rate, but a direct result of the application of the new adopted relations of the mass-loss rates. Near the Humphreys–Davidson limit, Γ_e rises close to 1 and, as described in Vink et al. (2011), when Γ_e is larger than 0.7, the mass-loss dependence on Γ_e becomes high and, correspondingly, the mass-loss rates are significantly enhanced. With this formulation, the boosting of the mass-loss rate at the highest masses ($M_{\text{ini}} \geq 150 M_{\odot}$) is effective already from the beginning of the main sequence and, because of the large mass-loss rates, they evolve almost downward vertically in the HR diagram. Interestingly, the luminosity of the tracks with the higher masses ($M_{\text{ini}} \geq 150 M_{\odot}$) falls with time much more than those of the less massive ones. This is caused by the overluminescence with respect to the main-sequence mass–luminosity relation which, being larger at larger masses, results in larger values of Γ_e . Thus, the evolved brightest massive stars are not necessarily those with the largest initial masses.

The Γ_e dependence of the mass-loss rates of O-type supergiant stars has not yet been studied for different galactic environmental conditions, apart from the analysis of the effects of CNO abundances (Muijres et al. 2012b). A more thorough analysis in a broad metallicity range, $10^{-3} Z_{\odot} \leq Z \leq 2 Z_{\odot}$, has been performed by

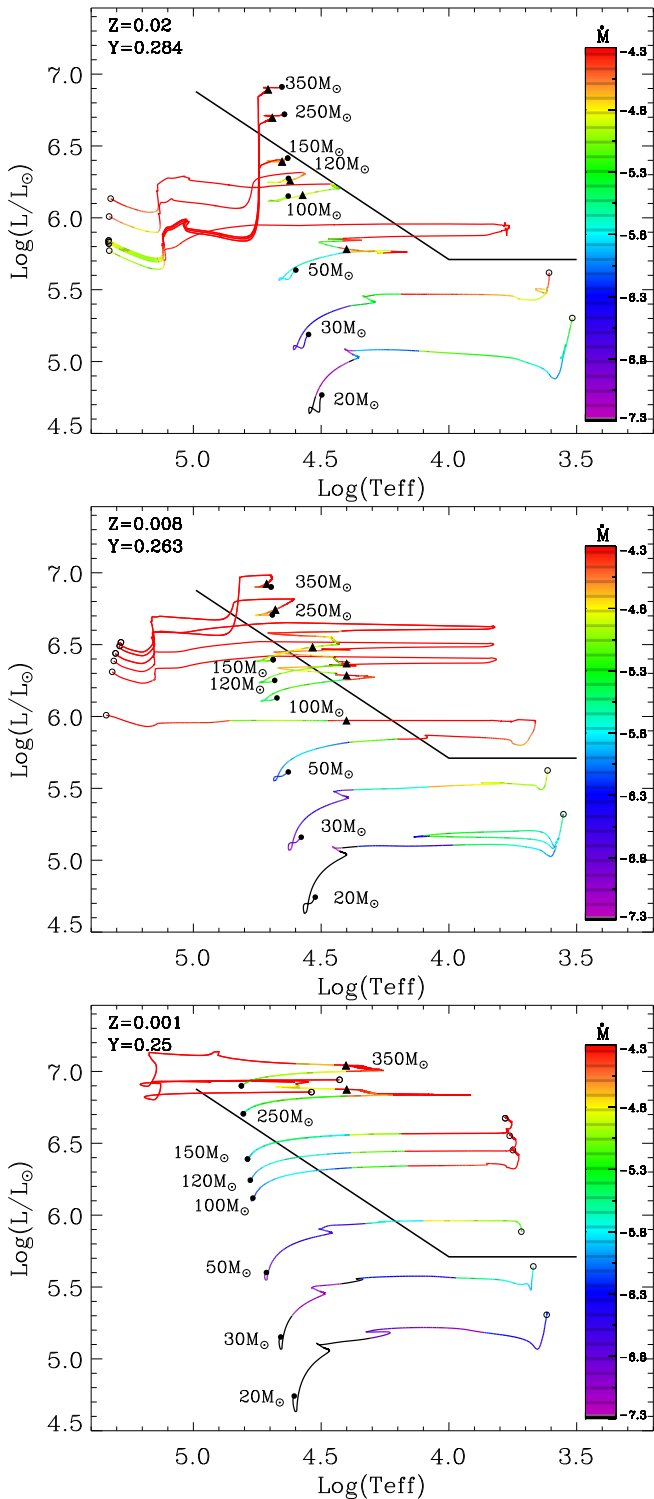


Figure 1. Selected evolutionary tracks for massive stars with $Z = 0.02$ (upper panel), $Z = 0.008$ (middle panel) and $Z = 0.001$ (lower panel). The mass-loss rates are indicated by the colour bar. The thick black straight lines represent the Humphreys–Davidson limit (Humphreys & Davidson 1979) which delimits the forbidden region above which only very few stars are observed in the HR diagram of the Galactic massive stars. The big solid and empty circles indicate the ZAMS and the end points of the tracks, respectively. The triangles mark the beginning of WR phase.

Gräfenner & Hamann (2008), but only for the case of WR stars. In particular, Gräfenner & Hamann (2008) show that the dependence of mass-loss rates on the metallicity is also a strong function of Γ_e . While at low values of Γ_e the mass-loss rates obey the relation of $\dot{M} \propto (Z/Z_\odot)^{0.85} M_\odot \text{ yr}^{-1}$, at increasing Γ_e the metallicity dependence decreases, and it disappears as Γ_e approaches 1. In the absence of a more comprehensive analysis of the dependence of the mass-loss rates on the metallicity and Γ_e , and since there is a continuity between the models provided by Vink et al. (2011) and those of WNL stars provided by Gräfenner & Hamann (2008, see discussion in Vink et al. 2011), we assume in PARSEC that the scaling with the metallicity obeys the following relation

$$\dot{M} \propto (Z/0.02)^\alpha \quad (2)$$

with the coefficient α determined from a rough fit to the published relationships by Gräfenner & Hamann (2008):

$$\alpha = 2.45 - 2.4 * \Gamma_e \quad (2/3 \leq \Gamma_e < 1) \quad (3)$$

and with the supplementary condition $0 < \alpha \leq 0.85$. In summary, our algorithm for the mass-loss is the following. Besides the already specified mass-loss rate formulations (R_{V01} , R_{dJ} and R_{NL}) we compute also R_{Γ_e} from the tables provided by Vink et al. (2011), but we scale the latter value with the metallicity, using equations (2) and (3). During the BSGs and LBVs phases the basic mass-loss rate adopted is R_{V01} . However, since, because of the effects of Γ_e , this can be encompassed by R_{Γ_e} and in order to secure a smooth transition, we adopt the maximum between R_{V01} and R_{Γ_e} . Towards the RSG phase we use R_{dJ} , but again, since this is an empirical rate parametrized in such a way that it should hold on a broad region of the HR diagram and it likely underestimates the mass-loss rates of luminous yellow supergiants (Salasnich et al. 1999), we compare it with R_{Γ_e} and take the maximum value. In the WR phases we consider the Nugis & Lamers (2000) formulation.

The HR diagram of a few selected evolutionary tracks for $Z = 0.008$ is shown in the middle panel of Fig. 1. We note here a significant decrease of the mass-loss rates, at a given mass. In particular while at $Z = 0.02$ the models of $M_{\text{ini}} \sim 120 M_\odot$ and $M_{\text{ini}} \sim 150 M_\odot$, rapidly turn their main-sequence evolution to higher effective temperatures, at $Z = 0.008$ the mass-loss rates are not high enough to prevent the tracks from entering into the forbidden region. Nevertheless, the tracks burn hydrogen around the Humphreys–Davidson limit until, near central helium ignition Γ_e becomes large and after performing a rapid excursion within the forbidden region, they turn into the blue part as WR stars. At even lower metallicities, the mass-loss rates decrease, unless the star is near the Eddington limit with $\Gamma_e \sim 1$, and the location of the predicted Humphreys–Davidson limit shifts to higher luminosities. For example, at $Z = 0.001$ in the lower panel of Fig. 1, the upper main sequence widens significantly and the more massive stars evolve into the ‘forbidden’ region even during the H-burning phase, because of their very large convective cores. They may also ignite and burn central helium as ‘red’ supergiant stars.

2.4 Comparison with previous releases

The current set of massive stars supersedes the old one adopted in several popular studies since 20 yr (Bressan et al. 1993; Fagotto et al. 1994, hereafter B93 and F94). With respect to B93 and F94, the new models have a significantly finer mass spacing and extend up to a higher upper mass limit. The computed masses range from 14 to 20 M_\odot in steps of 2 M_\odot , then up to 100 M_\odot in steps of 5 M_\odot and finally 120, 150, 200, 250, 300, 350 M_\odot . This allows for a quite

better interpolation in ages and masses and a sampling of different initial mass function up to larger initial masses. Simple stellar populations can now be sampled with a higher accuracy than before and with more suitable mass and time-steps. The new tracks include also the pre-main-sequence phase that begins when the central temperature of the protostar becomes larger than $\log(T_c/K) = 5.3$. No mass accretion is accounted for during the pre-main-sequence phase.

To summarize the differences brought by the adoption of the updated physics input we compare the new tracks with those of the previous PADOVA release, in the upper and middle panels of Fig. 2, for $Z = 0.02$ and $Z = 0.008$, respectively. Besides the presence of the pre-main sequence in the new tracks, which for purposes of clarity is not shown, a few general trends can be seen in the figure. At $Z = 0.02$, the zero-age main sequence (ZAMS) is similar. Note that the old tracks do not include the pre-main-sequence phase. The main sequence termination is only slightly hotter in the new tracks, likely because of differences in the underlying opacities. The RSG phase is slightly cooler in the new tracks, but the differences are barely significant. We remind that in B93 and F94 the density inversion (arising in the inefficient region of the convective envelope) was inhibited in the computation of massive star tracks. In a later revision of the tracks (Girardi et al. 2000) it was inhibited at all masses. As discussed in Alongi et al. (1993), a density inversion may develop in the external inefficient convection zones because of the requirement of the hydrostatic equilibrium in a region with a large superadiabatic real temperature gradient (assuming typical values of the mixing length parameter). This situation which should lead to a Rayleigh–Taylor instability or even a significant increase in the mass-loss rate, may give rise to numerical instabilities which preclude the computation of the track. To inhibit the density inversion one may use a mixing length parameter proportional to the density scaleheight (H_ρ) which, by rendering convection more efficient in the region where the density has a relative maximum, prevents a large superadiabatic real temperature gradient. Alternatively one may impose that the real temperature gradient is limited by $\nabla_T \leq \nabla_{T_{\max}} = \frac{1-\chi_\mu \nabla_\mu}{\chi T}$, which is the choice made since B93 and F94. This also simulates a more efficient convection and prevents the development of numerical instabilities. However, since a larger convective efficiency results in a hotter red giant track, and since B93 and F94 red giant tracks of intermediate and low-mass stars compared well with the corresponding observed colours, we follow their method and inhibit density inversion only for the most massive stars. Thus, the most massive RSG have effective temperatures that are slightly hotter than those obtained by allowing density inversion to occur. A detailed analysis of this effect is clearly needed, but likely it must also take into account effects of dusty circumstellar envelopes which are known to affect the colours of RSG stars.

The mass-loss rates adopted here are less efficient already at $M_{\text{ini}} = 30 M_\odot$. At this mass, the star ignites carbon as a red giant while in B93 and F94 the star is already moving towards the hot region of the HR diagram. This effect is more striking in the more massive stars, for those reaching the WR stages. Comparing the two models of $60 M_\odot$ we see that while the H-burning and the central helium ignition phases are pretty similar, the final WR phase is very different. The mass-loss adopted for the WR stages in B93 and F94 is significantly larger than that adopted here and the star ends with a luminosity which is about one order of magnitude lower. At higher masses, $M_{\text{ini}} = 100$ and $120 M_\odot$, there are significant differences already in the core H-burning. The mass-loss rates are initially higher in the B93 and F94 models, but when the effects of Γ_e become important, the mass-loss rates become comparable

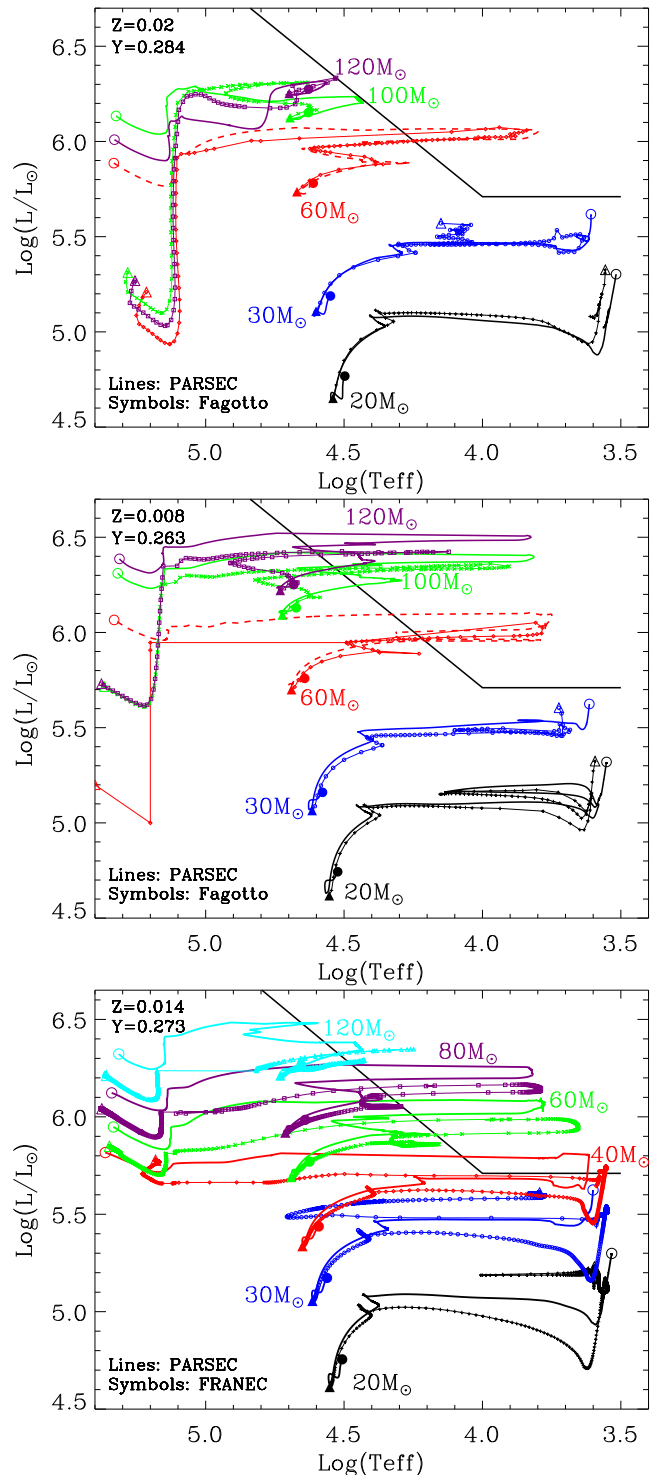


Figure 2. Upper and middle panels: comparison with previous releases of PADOVA evolutionary tracks (symbols, Bressan et al. 1993; Fagotto et al. 1994) with $Z = 0.02$ (upper panel) and $Z = 0.008$ (middle panel). Models of different masses are indicated with different colours and line styles/symbols. Note that helium abundances are $Y = 0.28$ for $Z = 0.02$ and $Y = 0.25$ for $Z = 0.008$ in Fagotto et al. (1994); Bressan et al. (1993). Lower panel: comparison with the FRANEC solar abundance ($Z = 0.01345$) models without rotation (symbols, Chieffi & Limongi 2013). The meaning of big circles is the same as in Fig. 1, while the big triangles are used for the alternative models. The Humphreys–Davidson limit is also drawn as in Fig. 1.

and the tracks evolve along the similar path. There remain a large difference in the mass-loss rate adopted in the advanced WR stages.

We stress again that in B93 and F94 models the mass-loss is arbitrarily enhanced when the stars approach or encompass the Humphreys–Davidson limit, while in the current models the mass-loss enhancement is a result of the photospheric conditions. In this respect, it is very interesting to note the similarity between the tracks of $M_{\text{ini}} = 60 M_{\odot}$ that can be taken as representative of the fact that the mass-loss enhancement is no more imposed as before, but it is instead a natural consequence of the *photospheric* conditions.

The comparisons with the models of $Z = 0.008$, typical of the LMC, confirm the previous picture. The ZAMS is pretty similar, but now the effects of a lower metallicity become visible, since the normalization metallicity for the mass-loss rate has been assumed to be $Z = 0.02$. In the old models, the metallicity dependence was slightly lower, $\dot{M} \propto (Z/0.02)^{0.5}$, and the mass-loss rates at $Z = 0.008$ were about 40 per cent larger than in the current models, keeping other parameters fixed. Thus, the new models evolve at slightly higher luminosity until the effects of Γ_e become important. Again there is a striking similarity in the turnover of the effective temperature in the models that overcome the Humphreys–Davidson limit. As before, in the final WR stages the stars evolve at a significantly higher luminosity than that of the old models. We note that, while in the advanced WR stages the luminosities of the new models are significantly higher, the corresponding lifetime is more or less unchanged (~ 0.1 Myr for $100 M_{\odot}$ models). This means that the new models should contribute far more to the hard ionizing photons than the old ones. This will be the subject of a forthcoming paper dedicated to the integrated properties of young star clusters. For the comparison with models by other groups, we select the evolutionary tracks without rotation computed with the FRANEC code (Chieffi & Limongi 2013). The HR diagram is shown in the lower panel of Fig. 2. The FRANEC models (dashed lines) are for a composition of $Z = 0.01345$ and $Y = 0.265$ while PARSEC models (solid lines) are for a slightly different chemical composition, $Z = 0.014$ and $Y = 0.273$. They adopt a mixing-length parameter $\alpha \equiv \Lambda/H_p = 2.3$ and a core overshooting region of $0.2H_p$ (Chieffi & Limongi 2013; Martins & Palacios 2013). One of the major difference is the presence of big blue loops in the FRANEC 20, 30 and $40 M_{\odot}$ models, while the big blue loops are absent in our models. In this respect, we note that the main sequence termination of our models is significantly cooler and more luminous than that of FRANEC models. This is particularly evident in the model of $M_{\text{ini}} = 40 M_{\odot}$ and it is indicative of a larger central mixing during the main-sequence phase of our models, which is known to disfavour the occurrence of blue loops. The larger extension of the loops in the FRANEC models could also be due to their use of the Ledoux criterion for the definition of the borders of the intermediate unstable regions. It is well known that the Ledoux criterion inhibits the development of the intermediate convective regions within the hydrogen profile, at the end of the H-burning phase, favouring a deeper penetration of the convective envelope when the stars move into the RSG region. This is an important issue deserving further investigation. Preliminary models computed adopting either the Schwarzschild or the Ledoux criterion in the hydrogen chemical composition profile, confirm that the main cause of the inhibition of blue loops is the extent of core overshooting (or another kind of extended mixing) during main hydrogen burning phase. With a slightly reduced core overshooting, also PARSEC models with the Schwarzschild criterion show extended blue loops (Tang et al. 2015, in preparation).

We also see that the behaviour of the tracks within the Humphreys–Davidson region is very similar. In both cases, the models abandon this forbidden region after losing a significant fraction of their mass. In both cases, the mass-loss must be enhanced, but the invoked mechanism are different: Chieffi & Limongi (2013) invoke the dust mass-loss enhancement (van Loon et al. 2005), while we invoke the Γ_e mass-loss enhancement.

3 STELLAR ATMOSPHERE MODELS

We convert from effective temperature, gravity and luminosity to magnitudes and colours using theoretical atmosphere models. Since one of our aims is to provide also isochrones in the observational plane, we need a full set of atmosphere models encompassing a wide range of parameters, i.e. masses, evolutionary stages and metallicities. In the following, we describe the different atmosphere models adopted. We begin with ATLAS models (Kurucz 1993; Castelli & Kurucz 2004), which are the canonical models suitable for intermediate and low-mass stars. We complement this library with our new calculations of wind models for hot massive stars with the WM-BASIC code (Pauldrach et al. 1986), and new models of WR stars from the Potsdam group (Gräfener et al. 2002; Hamann & Gräfener 2003, 2004; Hamann et al. 2006; Sander et al. 2012; Hainich et al. 2014). For the coolest stars we adopt the PHOENIX models (Allard et al. 1997), already extensively discussed in our previous paper (Chen et al. 2014).

3.1 Intermediate mass and low-mass stars

The core of our library consists of the plane parallel ATLAS9 models (Kurucz 1993). These LTE (local thermal equilibrium) models are well suited to describe the atmospheres of intermediate and low-mass stars of spectral type between A and K. The most recent ATLAS9 models are those computed by Castelli & Kurucz 2004. ATLAS9 models are based on the solar abundances by GS98 and make use of an improved set of molecular lines including TiO, H₂O, H₁–H₁ and HI–H⁺. The model grids are computed for T_{eff} from 3500 to 50 000 K, $\log g$ from 0.0 to 5.0 dex and $[M/H] = +0.5, +0.2, 0.0, -0.5, -1.0, -1.5, -2.0, -2.5, -3.5, -4$ and -5.5 . We limit the use of ATLAS9 models to the temperature range of $19\,000\text{ K} > T_{\text{eff}} > 6000\text{ K}$. At higher temperature in general we need to consider models with mass-loss while at lower temperature the PHOENIX models are more appropriate.

3.2 Hot massive stars

O, B stars. For temperatures typical of O and B stars ($60\,000\text{ K} > T_{\text{eff}} > 19\,000\text{ K}$) we have generated a new library of models using the public code WM-BASIC (Pauldrach et al. 1986). This allows us to take into account both the effects of extended winds and those of non-LTE, since both effects may significantly affect the emergent spectra of hot stars. We have generated new sets of stellar spectral libraries covering as much as possible the space of parameters of our new evolutionary tracks of massive stars, i.e. effective temperature, gravity, metallicity and mass-loss rate. The temperature grid ranges from $\log T_{\text{eff}} = 4.3$ to 5.0 in steps of $\Delta \log T_{\text{eff}} = 0.025$ dex. At each temperature, we adopt a step in gravity of $\Delta \log g = 0.5$ dex, with upper and the lower boundaries that depend on the T_{eff} . Indeed, the highest gravity is determined by the fact that the line-driven radiation force cannot initiate the stellar wind, while the lowest value corresponds to stability problems when the models approach

the Eddington limit. At each grid point we consider three different values of the mass-loss rates, $\dot{M} = 10^{-7}$, 10^{-6} , and $10^{-5} M_{\odot} \text{ yr}^{-1}$, encompassing typical values for O, B stars. We note that, besides T_{eff} , $\log g$ and stellar radius (radius defined at a Rosseland optical depth of $2/3$, $R_{\tau=2/3}$), there are additional input parameters in WM-BASIC, κ , α and δ , referring most specifically to the structure of the wind as shown by Castor et al. (1975). Thus, for any point in the (effective temperature, gravity) grid we suitably change the other stellar parameters (radius, luminosity and mass) as well as the wind parameters α and κ in order to obtain three consistent atmosphere models with the required values of mass-loss rate, $\dot{M} = 10^{-7}$, 10^{-6} , $10^{-5} M_{\odot} \text{ yr}^{-1}$. These models are used to derive the broad-band colours and magnitudes for any given effective temperature, gravity and metallicity, easily interpolating for the different values of the mass-loss rate actually used in the tracks. Our new library consists of about 300 models for each metallicity. For example for $z = 0.02$, we computed 105 models for $\dot{M} = 10^{-7} M_{\odot} \text{ yr}^{-1}$, 98 for $\dot{M} = 10^{-6} M_{\odot} \text{ yr}^{-1}$ and 86 for $\dot{M} = 10^{-5} M_{\odot} \text{ yr}^{-1}$. The metal partition adopted in the new models is the same as used in Bressan et al. (2012), to say Caffau et al. (2011). As an example, we show in Fig. 3, the effects of changing the mass-loss rate at constant metallicity (upper panel) and those of changing the metallicity at constant mass-loss rate (lower panel), for models with $\log T_{\text{eff}} = 4.6$ and $\log g = 3.5$. In the upper panel, the black solid line refers to the model with $\dot{M} = 10^{-5} M_{\odot} \text{ yr}^{-1}$, while the red dotted one is for $\dot{M} = 10^{-7} M_{\odot} \text{ yr}^{-1}$. We can see that the He II continuum is more absorbed in the model with higher mass-loss rate. We notice also that, as expected, some spectral features which appears in emission in the higher mass-loss rate model, turn into absorption in the model with a lower mass-loss rate.

In the lower panel, the black solid line refers to the same model as in the upper panel, while, the red dotted one is now for a model at the same grid point but with $Z = 0.008$. This comparison shows that the effects of changing the metallicity on these hot spectra are less pronounced than those arising from the variation of the mass-loss rates.

WR stars. WR stars typically have wind densities one order of magnitude larger than those of massive O-type stars. Spectroscopically they are dominated by the presence of strong broad emission lines of helium, nitrogen, carbon and oxygen. They are subdivided into different subtypes, one with strong lines of helium and nitrogen (WN stars), another one with strong lines of helium and carbon (WC stars) and a third one with strong oxygen lines (WO stars).

To reproduce their spectra we make use of the most recent library of WR models computed by the Potsdam group (POWR; Gräfener et al. 2002; Hamann & Gräfener 2003, 2004; Hamann et al. 2006; Sander et al. 2012; Hainich et al. 2014). They provide models with metallicities corresponding to those of WR stars in the Galaxy, the Large Magellanic Cloud (LMC) and the Small Magellanic Cloud (SMC). The model grids are parametrized with $T_{\text{eff}, \tau=20}$ (the effective temperature at radius where the Rosseland optical depth is 20), and the transformed radius R_t (because models with the same set of such parameters show the same emergent spectrum as discussed in Schmutz, Leitherer & Gruenwald 1992). The transformed radius R_t is given by (Schmutz, Hamann & Wessolowski 1989):

$$R_t = R_{\tau=20}^* \left(\frac{v_{\infty}}{2500 \text{ km s}^{-1}} \frac{10^{-4} M_{\odot} \text{ yr}^{-1}}{\dot{M}} \right)^{2/3}. \quad (4)$$

Since $R_{\tau=20}^*$ is nearly equivalent to the hydrostatic radius of the evolutionary tracks, this quantity combines stellar radius and mass-loss rate of the tracks with the terminal velocity. For the same reason

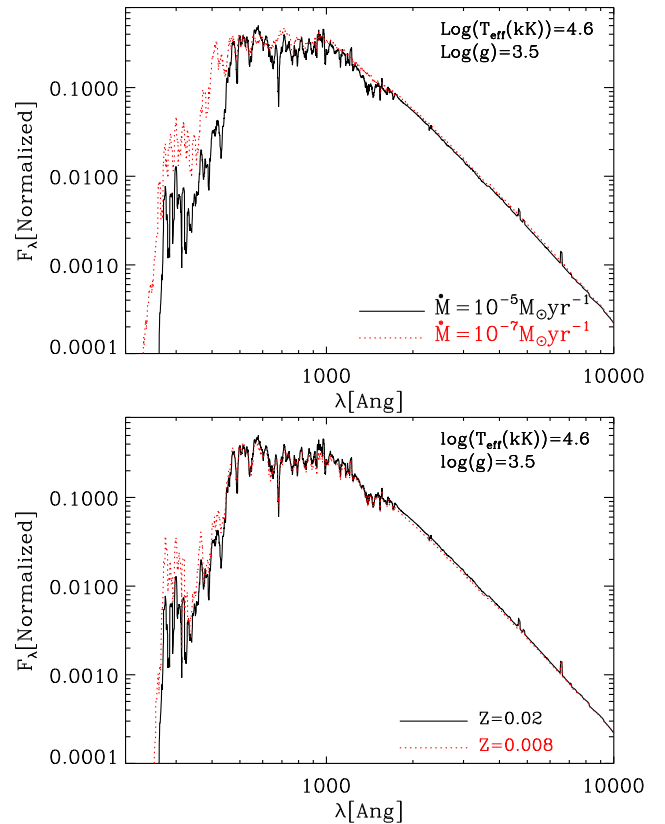


Figure 3. Upper panel: comparison of WM-BASIC spectra (smoothed) with different mass-loss rates. The effective temperature, gravity, radius and metallicity ($Z = 0.02$) are the same, but the black solid line is for $\dot{M} = 10^{-5} M_{\odot} \text{ yr}^{-1}$ and the red dotted line is for $\dot{M} = 10^{-7} M_{\odot} \text{ yr}^{-1}$. The ionizing photon (with wavelength less than 912 nm) number ratio ($N_{\text{ionizing}}(\dot{M} = 10^{-5} M_{\odot} \text{ yr}^{-1})/N_{\text{ionizing}}(\dot{M} = 10^{-7} M_{\odot} \text{ yr}^{-1})$) supposing the same luminosity is 0.197. Lower panel: comparison of WM-BASIC spectra (smoothed) with different metallicities. The effective temperature, gravity, radius and mass-loss rate ($\dot{M} = 10^{-5} M_{\odot} \text{ yr}^{-1}$) are the same, but the black solid line is for $Z = 0.02$ and the red dotted line is for $Z = 0.008$. The ionizing photon number ratio ($N_{\text{ionizing}}(Z = 0.02)/N_{\text{ionizing}}(Z = 0.008)$) supposing the same luminosity is 0.994 (almost identical). All the spectra are normalized over the wavelength range from 0.84 to 1.44 μm .

$T_{\text{eff}, \tau=20}$ corresponds to the effective temperature of our hydrostatic models T_{eff}^* . As shown in Hamann & Gräfener (2004), at large R_t (or thin winds), $T_{\text{eff}, \tau=20} \simeq T_{\text{eff}, \tau=2/3}$. (In the case of our WM-BASIC models, R_t are always $\gtrsim 1.5$, so there is no need to use R_t to match atmosphere models and theoretical tracks.) As done in Schmutz et al. (1992), we match the WR atmospheres to the evolutionary tracks by interpolating T_{eff}^* and R_t .

While the observational classification is quite well defined (Crowther, De Marco & Barlow 1998; Crowther 2007), it is more difficult to assign the WR subgroups along the evolutionary tracks. We use the following convention to identify them. WR stars are classified as WNL (late) when the surface hydrogen content X_{H} is below a given threshold, X_{WNL} . When $X_{\text{H}} = 0$, they are classified as WNE (early) if $N(^{12}\text{C}) < N(^{14}\text{N})$ and as WC if $N(^{12}\text{C}) \geq N(^{14}\text{N})$. We finally assign the WO subtype when the condition $N(^{12}\text{C}) + N(^{16}\text{O}) > N(^4\text{He})$ is fulfilled (Smith & Maeder 1991). We then match our type assignments with the models provided by POWR, which adopt a fixed composition for any given subtype. For example, for the Galactic metallicity, in the POWR

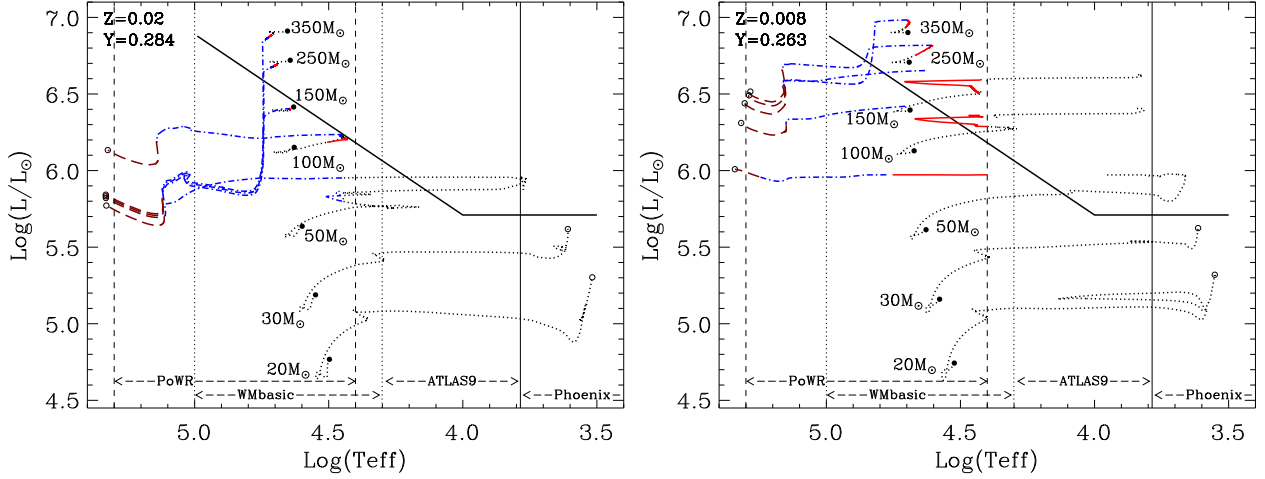


Figure 4. Evolutionary tracks for massive stars with $Z = 0.02$ (left-hand panel) and $Z = 0.008$ (right-hand panel). Different colours represent different evolutionary stages: black dotted lines for stages precedent of WR phases, red solid lines for models using POWR WNL-H50 ($Z = 0.02$) or WNL-H40 ($Z = 0.008$), blue dash–dotted lines for WN models, and brown dashed lines for WC models. The meaning of big circles is the same as in Fig. 1. The overplotted vertical lines delimit the coverages of different atmosphere models as indicated in the plots. The Humphreys–Davidson limit is also drawn as in Fig. 1.

library $X_{\text{WNL}} = 0.5$ and the different subtypes have the following surface compositions.

- (i) WNL-H50 for $X_{\text{H}} = X_{\text{WNL}}$, $X_{\text{He}} = 0.48$, $X_{\text{C}} = 1\text{E-}4$, $X_{\text{N}} = 0.015$, $X_{\text{O}} = 0$ and $X_{\text{Fe}} = 0.0014$;
- (ii) WNL for $X_{\text{H}} = 0.2$, $X_{\text{He}} = 0.78$, $X_{\text{C}} = 1\text{E-}4$, $X_{\text{N}} = 0.015$, $X_{\text{O}} = 0$ and $X_{\text{Fe}} = 0.0014$;
- (iii) WNE for $X_{\text{H}} = 0$, $X_{\text{He}} = 0.98$, $X_{\text{C}} = 1\text{E-}4$, $X_{\text{N}} = 0.015$, $X_{\text{O}} = 0$ and $X_{\text{Fe}} = 0.0014$;
- (iv) WC for $X_{\text{H}} = 0$, $X_{\text{He}} = 0.55$, $X_{\text{C}} = 0.4$, $X_{\text{N}} = 0$, $X_{\text{O}} = 0.05$ and $X_{\text{Fe}} = 0.0016$.

For the LMC, the surface hydrogen threshold is $X_{\text{WNL}} = 0.4$, while for the SMC they provide models with both $X_{\text{WNL}} = 0.6$ (WNL-H60 models) and $X_{\text{WNL}} = 0.4$ (WNL-H40 models). Note that POWR does not yet provide spectral models for WO stars, which, however, are quite rare objects especially at lower metallicities.

3.3 Cool stars

As reviewed by Allard et al. (1997), the atmospheres of cool stars are dominated by the formation of molecules and eventually at very low temperatures by dust condensation that can affect the spectral shape significantly. A suitable set of 1D, static spherical atmosphere spectral models accounting for the above effects has been developed in the recent years and is continuously maintained by the PHOENIX group (Allard et al. 2012). Among the different suites of libraries, we use the BT-SETTL models which contain the most updated and complete stellar parameter grid and are well tested against observations (Allard et al. 2012). The full BT-SETTL models are provided for $2600 \leq T_{\text{eff}} < 50\,000$ K, $0.5 < \log g < 6$, and metallicities $0.000\,003 \lesssim Z \lesssim 0.04$. We adopt such models for temperatures $T_{\text{eff}} \leq 6000$ K. These tables for cool stars have already been used in Chen et al. (2014), in the context of low and very low mass stars.

3.4 Synthetic BC_{λ} tables

A concern for the libraries described above is that the different sets (WM-BASIC, POWR, ATLAS9 and BT-SETTL) are calculated with different

metallicities and different partitions of heavy elements. In order to obtain homogeneous spectral libraries, at least as far as the metallicity is concerned, we first calculate the global metallicity from the detailed abundance values provided by each group. We note, for example, that the BT-SETTL models adopt a solar partition (Asplund et al. 2009) different from the one adopted in PARSEC (Caffau et al. 2011) and that, at low metallicities, their partitions are α enhanced. On the contrary, for our WM-BASIC models, we use the same metallicities as in PARSEC. We then interpolate each set of spectra on the global metallicity grid defined by the PARSEC models. Since POWR models are provided only for three typical metallicities, our Galaxy, the LMC and the SMC, we use Galaxy models for $Z \geq 0.01$, LMC models for $0.01 > Z > 0.006$ and SMC models for $Z \leq 0.006$. Unfortunately this procedure may introduce some error because the partition of heavy elements is not the same in the different libraries. For example when we re-scale the Caffau et al. (2011) and the GS98 partitions to a metallicity of $Z = 0.02$, we find a difference of ~ 17 per cent in the iron content and ~ 5 per cent in the oxygen content. However, we verified that these variations have negligible effects on the broad-band colours of hot spectra. On the other hand this is the best one can do until a homogeneous set of model atmospheres (i.e. with the same partition of heavy elements) is computed on a range of parameters broad enough. The ranges of effective temperatures encompassed by different spectral libraries are marked by vertical lines in the HR diagrams shown in Fig. 4, for $Z = 0.02$ (left-hand panel) and $Z = 0.008$ (right-hand panel), respectively. Overplotted are selected stellar evolutionary tracks from $M_{\text{ini}} = 20 M_{\odot}$ to $M_{\text{ini}} = 350 M_{\odot}$. The combined atmosphere models, that share the same global metallicity of the corresponding evolutionary tracks as shown in the HR diagram, provide a very good coverage in terms of effective temperatures and gravities. They allow for an optimal calculation of BC_{λ} tables that are used to convert from theoretical to observational diagrams. The details of this process are thoroughly described in Girardi et al. (2002) and Chen et al. (2014), and are not repeated here. While for the evolutionary tracks we only consider the photospheric magnitudes, the corresponding isochrones also account for the effect of possible circumstellar dusty envelopes following the dust calculation recipes described in Marigo et al. (2008) and Nanni et al. (2013, 2014).

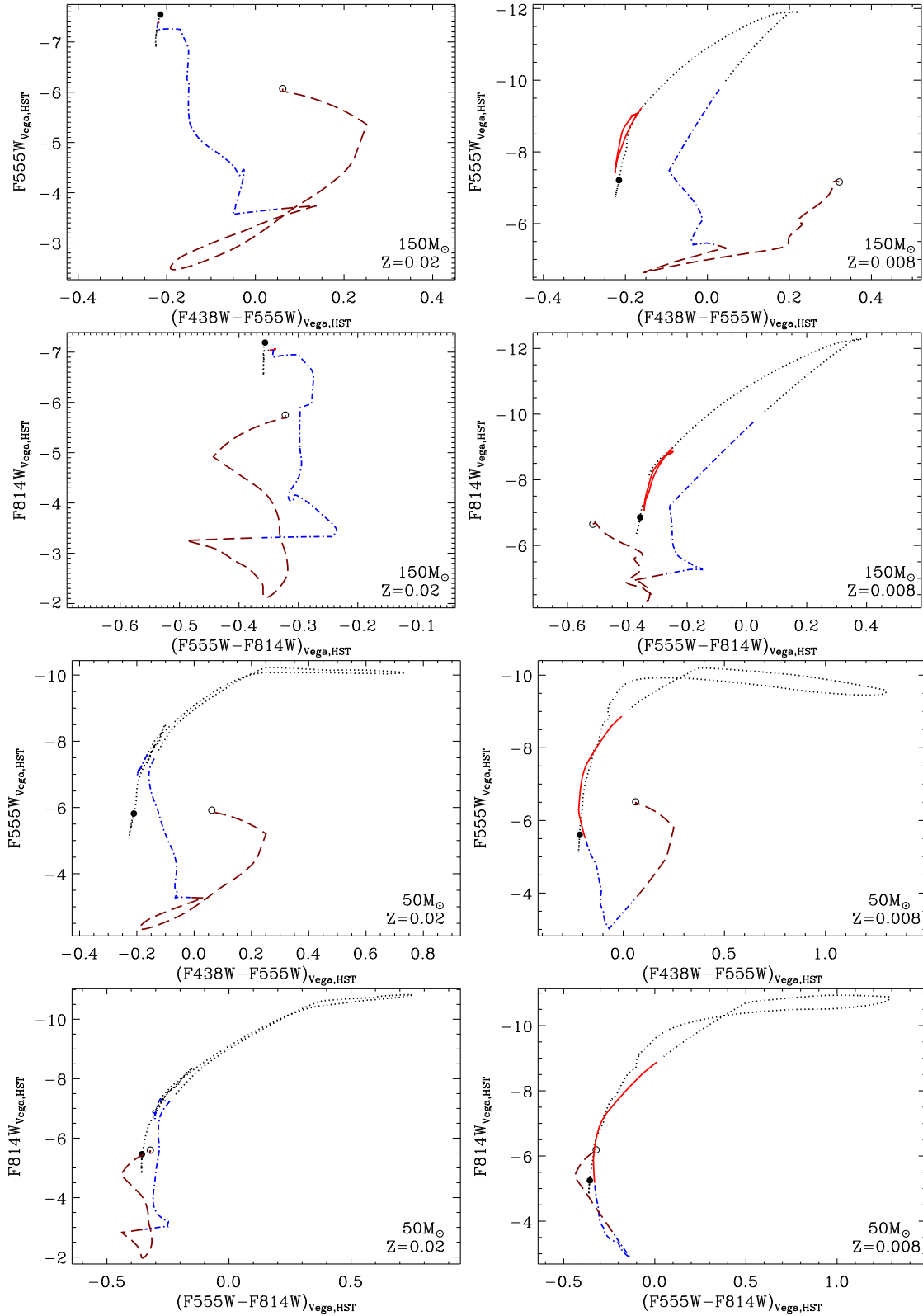


Figure 5. Colour–magnitude diagrams in *HST*/Wide Field Camera 3 (WFC3) broad-bands for tracks of $M_{\text{ini}} = 150 M_{\odot}$ (upper four panels) and $M_{\text{ini}} = 50 M_{\odot}$ (lower four panels) with $Z = 0.02$ (left-hand panels) and $Z = 0.008$ (right-hand panels), respectively. The meaning of colours and line styles along the tracks is the same as in Fig. 4. The meaning of big circles is the same as in Fig. 1.

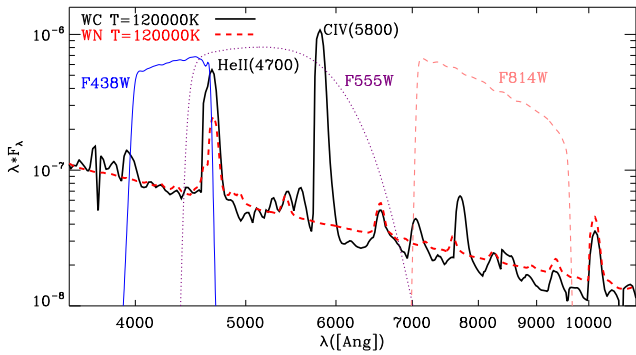


Figure 6. Comparison of CMFGEN (Hillier & Miller 1998) WC and WN models with the same effective temperature $T_{\text{eff}} = 120\,000\text{ K}$ and metallicity $Z = 0.02$. Also shown are the transmission curves of three *HST*/WFC3 filters (F438W, F555W and F814W). Note that the two strong emission lines He II(4700) and C IV(5800) can greatly influence the magnitude/colours in related passbands.

4 DISCUSSIONS AND CONCLUSIONS

We present new evolutionary tracks of massive stars for a broad range of metallicities, $0.0001 \leq Z \leq 0.04$ and for initial masses up to $M_{\text{ini}} = 350 M_{\odot}$. At supersolar metallicity, the models extend up to $M_{\text{ini}} = 200 M_{\odot}$ ($Z = 0.03$) and $M_{\text{ini}} = 150 M_{\odot}$ ($Z = 0.04$), respectively. The new models complement the already published PARSEC data base (Bressan et al. 2012) and supersede the old PADOVA evolutionary tracks of massive stars which are more than 20 yr old. The stellar models are evolved from the pre-main-sequence phase to the central carbon ignition. The mass grid is very well sampled and it is fully adequate to perform detailed investigations of very young stellar systems both from the point of view of the resolved populations and from their integrated properties.

We revise the scheme adopted for including the mass-loss rate in the evolution of massive stars, by combining recent recipes found in the literature. Among the new recipes, particularly important is the enhancement of the mass-loss rate when the luminosity approaches the Eddington limit. We show that with the recent formulation by Vink et al. (2011), the models naturally reproduce the observed Humphreys–Davidson limit observed in the Galactic and LMC HR diagrams. In previous PADOVA models this limit was used as a threshold to enhance the mass-loss rates, independently from the metal-

licity. In this paper, the role of the metallicity is described by means of a simple recipe derived from the models presented in Gräfenr & Hamann (2008). The metallicity dependence of the mass-loss rate is now described by a power law with an exponent α which depends on Γ_e (equation 1), the ratio between the stellar luminosity and the Eddington luminosity. When Γ_e approaches unity the metallicity dependence drops significantly, allowing for relatively high mass-loss rates also in stars of low metallicity. At lower values of Γ_e the usual exponent is recovered, $\alpha = 0.85$. While the models of Gräfenr & Hamann (2008) refer particularly to the WR phase, it has already been shown that there is a continuity between the new Vink et al. (2011) formalism and the Gräfenr & Hamann (2008) results for WNL stars. The result of the new mass-loss formulation is that the Humphreys–Davidson limit shows a clear dependence with metallicity and it even disappears at very low metallicities.

Compared to our previous models with the same metallicity (Bressan et al. 1993; Fagotto et al. 1994), the major difference concerns the WR phases. The new models evolve in the late WR stage, at $\log T_{\text{eff}} > 5.0$, with luminosities which are significantly higher than those of the old PADOVA tracks (~ 0.9 dex in $\log(L/L_{\odot})$). These differences result from the different mass-loss recipes used in the advanced WR phases. Since the lifetimes of the models in this phase remain more or less the same, the new models should contribute much more to the hard ionizing photons. At lower metallicity, $Z \leq 0.008$, the new mass-loss formulation introduces significant differences even in the earlier phases. Our models compare well with the recent evolutionary tracks of non-rotating stars of similar metallicity, computed with FRANEC (Chieffi & Limongi 2013).

Besides evolutionary tracks, we provide new tables of BC_{λ} that allow for the conversion from the theoretical HR to the observed colour–magnitude diagrams. For this purpose, we assemble existing atmosphere libraries, ATLAS9, POWR, PHOENIX and new atmosphere models calculated on purpose with the WM-BASIC code. We merge the different libraries with interpolation on a global metallicity scale, providing quite homogeneous tables of BC_{λ} , at several metallicities.

An example of the colour–magnitude diagrams of the tracks of $M_{\text{ini}} = 100 M_{\odot}$ and $M_{\text{ini}} = 50 M_{\odot}$ is shown in Fig. 5, for $Z = 0.02$ (left-hand panels) and $Z = 0.008$ (right-hand panels), respectively. In the figure, we highlight the different evolutionary phases with different colours and line styles. Black dotted lines indicate the evolution precedent of the WR stages, while the red solid lines are used to indicate the transition phase from the LBV phase to the late

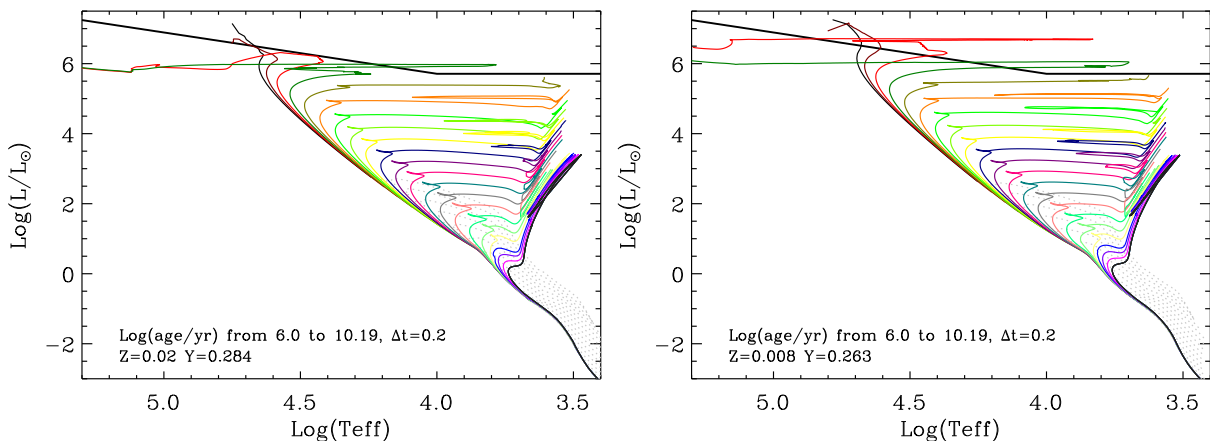


Figure 7. Isochrones of different ages, as indicated by the labels, are shown for $Z = 0.02$ (left-hand panel) and $Z = 0.008$ (right-hand panel). Note that at young ages the intermediate and low-mass stars are still on the pre-main sequence (grey dotted lines). The Humphreys–Davidson limit is also drawn as in Fig. 1.

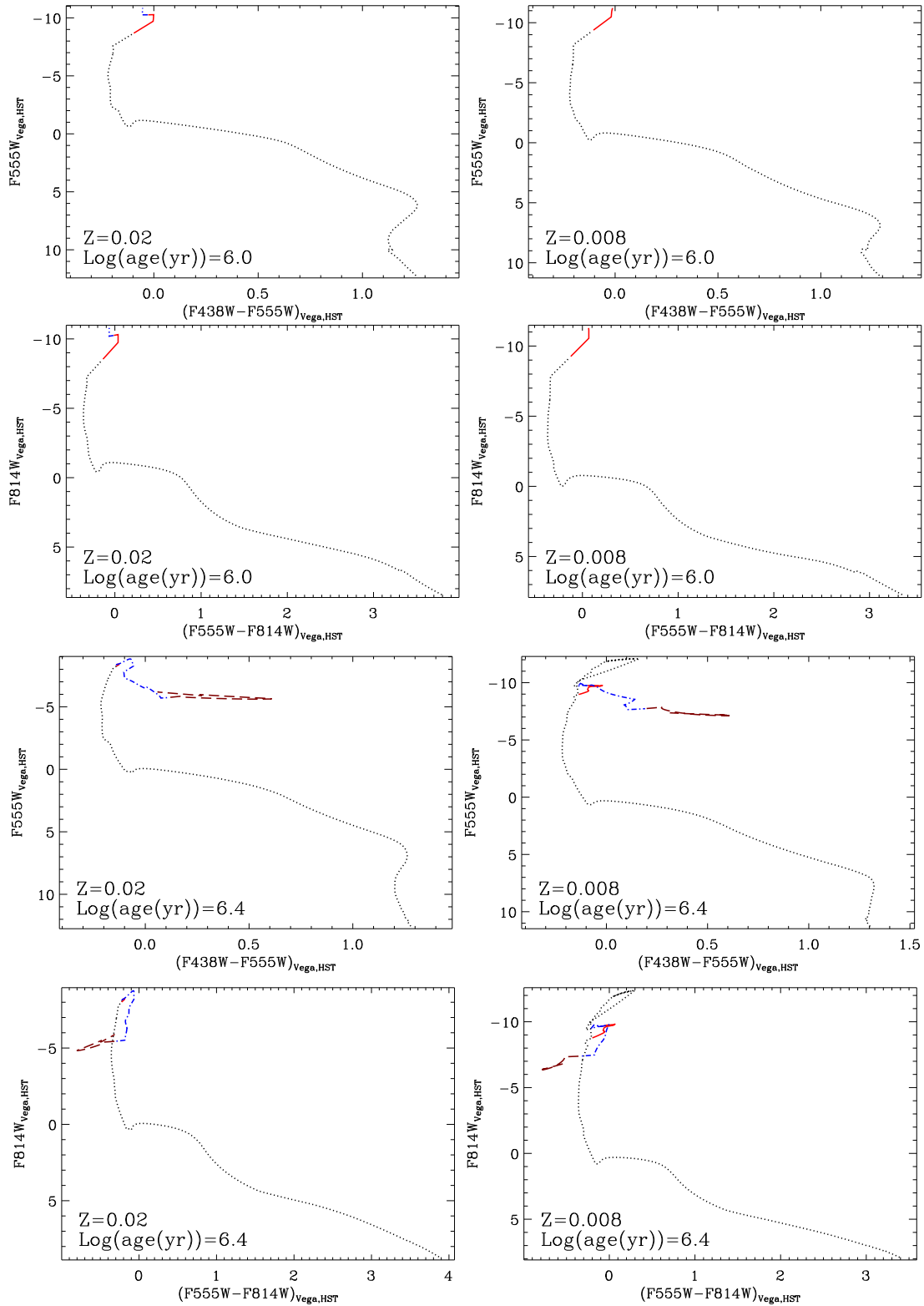


Figure 8. Colour–magnitude diagrams in *HST*/WFC3 broad-bands for isochrones of 1 Myr (upper four panels) and 2.5 Myr (lower four panels) with $Z = 0.02$ (left-hand panels) and $Z = 0.008$ (right-hand panels). The meaning of colours and line styles along the isochrones is the same as in Fig. 4.

WR stars (WNL-H50 for $Z = 0.02$ or WNL-H40 for $Z = 0.008$ in the POWR notation). The blue dash–dotted lines are used for the other WN stages and the brown dashed lines are for the final WC/WO stages.

As can be seen in the figure, the optical colours show some evident jumps when the star type changes from WN to WC. This is likely to be caused by the appearance of different strong emission lines in different subtypes. This can be seen from Fig. 6, where

we compare the spectra of one WC star (black solid line) and one WN (red dashed line) star with the same effective temperature. We show the optical region sampled by the broad-band filters $F438W$, $F555W$ and $F814W$ of the *HST*/WFC3 system. To better clarify this point we have used in the comparison the high resolution $CMFGEN$ spectra (Hillier & Miller 1998), which better show how the emission lines affect the spectra and the broad-band colours. Both spectra show a strong emission $He\ II(4700\ \text{\AA})$ line, falling within the $F555W$ passband and touching the border of the $F438W$ passband. The differences between the WN and the WC spectral types are mainly on the contribution of the strong $C\ IV(5800\ \text{\AA})$ line within the $F555W$ passband, in the latter type. Thus, the flux in the $F555W$ passband is heavily enhanced in the case of the WC star with respect to that of the WN star, and correspondingly the sudden transition from the WN to the WC types is accompanied by a jump in the $F438W$ – $F555W$ and $F555W$ – $F814W$ colours. It is important to stress that the $C\ IV(5800\ \text{\AA})$ doublet is very sensitive to the adopted atmosphere parameters which somehow challenges its predictability (Todt, Hamann & Gräfener, private communication). Furthermore, we have to note that the transition between WN and WC spectral types is smoother in the tracks than in the spectra, because the latter are computed only at discrete values of the elemental abundances, and this could enhance the effect, at least in terms of evolutionary speed.

Using the evolutionary tracks we compute new isochrones of young stellar populations, with the same procedure already described in Bressan et al. (2012). A few examples are shown in the theoretical HR diagram of Fig. 7, from very young to very old ages and for $Z = 0.02$ (left-hand panel) and $Z = 0.008$ (right-hand panel), respectively. By means of the new BC_λ tables, we convert theoretical isochrones into observational magnitudes/colours, in the same way used for the evolutionary tracks. In Fig. 8, we show the colour–magnitude diagrams of isochrones at very young ages, 1 and 2.5 Myr, and for $Z = 0.02$ and $Z = 0.008$. The colour codings are the same as in Fig. 5, but for the pre-main sequence which is drawn in light grey.

A preliminary comparison of the new models with the colour–magnitude diagrams of star-forming regions in nearby low metallicity dwarf irregular galaxies, has already been performed in Tang et al. (2014). The new models of massive stars will be used to compute the integrated properties of young star-forming regions (Obi et al., in preparation). The full sets of evolutionary tracks can be downloaded from <http://people.sissa.it/~sbressan/parsec.html>. The isochrones can be downloaded from <http://stev.oapd.inaf.it/cgi-bin/cmd>.

ACKNOWLEDGEMENTS

We thank the anonymous referee for the suggestions which helped to improve the paper. We thank A. W. A. Pauldrach for the help on running *WM-BASIC*, D. J. Hillier for the help with the *CMFGEN* code, M. Limongi for providing their tracks. We specially thank H. Todt, W.-R. Hamann and G. Gräfener for their extensive help on the *POWER* data base. We thank S. Charlot, X. T. Fu and Z. Y. Zhang for helpful discussions. YC and AB, and LG acknowledge the financial support from INAF through grants PRIN-INAF-2014-14. AB, LG and PM acknowledge the support from the ERC Consolidator Grant funding scheme (*project STARKEY*, G.A. no. 615604). PM acknowledges the support from the University of Padova, (*Progetto di Ateneo 2012*, ID: CPDA125588/12). XK and YC acknowledge financial supports from the National Natural Science Foundation of China (NSFC, nos. 11225315, 1320101002, 11433005 and 11421303),

the Strategic Priority Research Program ‘The Emergence of Cosmological Structures’ of the Chinese Academy of Sciences (no. XDB09000000), the Specialized Research Fund for the Doctoral Program of Higher Education (SRFDP, no. 20123402110037), and the Chinese National 973 Fundamental Science Programs (973 program) (2015CB857004).

This research has made use of NASA’s Astrophysics Data System Bibliographic Services.

REFERENCES

- Allard F., Hauschildt P. H., Alexander D. R., Starrfield S., 1997, *ARA&A*, 35, 137
- Allard F., Homeier D., Freytag B., Sharp C. M., 2012, *EAS Publ. Ser.*, 57, 3
- Alongi M., Bertelli G., Bressan A., Chiosi C., 1991, *A&A*, 244, 95
- Alongi M., Bertelli G., Bressan A., Chiosi C., Fagotto F., Greggio L., Nasi E., 1993, *A&AS*, 97, 851
- Asplund M., Grevesse N., Sauval A. J., Scott P., 2009, *ARA&A*, 47, 481
- Barsukova E. A., Goranskij V. P., Valeev A. F., Kaisin S. S., 2014, preprint ([arXiv:1412.7090](https://arxiv.org/abs/1412.7090))
- Bertelli G., Nasi E., Girardi L., Marigo P., 2009, *A&A*, 508, 355
- Böhm-Vitense E., 1958, *ZAp*, 46, 108
- Bressan A. G., Chiosi C., Bertelli G., 1981, *A&A*, 102, 25
- Bressan A., Fagotto F., Bertelli G., Chiosi C., 1993, *A&AS*, 100, 647 (B93)
- Bressan A., Marigo P., Girardi L., Salasnich B., Dal Cero C., Rubele S., Nanni A., 2012, *MNRAS*, 427, 127
- Bressan A., Marigo P., Girardi L., Nanni A., Rubele S., 2013, in Montalbán J., Noels A., Van Grootel V., eds, *EPJ Web Conf.*, Vol. 43, Liège, Belgium, p. 3001
- Brott I. et al., 2011, *A&A*, 530, A115
- Bruzual G., Charlot S., 2003, *MNRAS*, 344, 1000
- Caffau E., Ludwig H.-G., Steffen M., Freytag B., Bonifacio P., 2011, *Sol. Phys.*, 268, 255
- Cai Z.-Y., Lapi A., Bressan A., De Zotti G., Negrello M., Danese L., 2014, *ApJ*, 785, 65
- Castelli F., Kurucz R. L., 2004, preprint ([astro-ph/0405087](https://arxiv.org/abs/astro-ph/0405087))
- Castor J. I., Abbott D. C., Klein R. I., 1975, *ApJ*, 195, 157
- Chen Y., Girardi L., Bressan A., Marigo P., Barbieri M., Kong X., 2014, *MNRAS*, 444, 2525
- Chieffi A., Limongi M., 2013, *ApJ*, 764, 21
- Crowther P. A., 2007, *ARA&A*, 45, 177
- Crowther P. A., De Marco O., Barlow M. J., 1998, *MNRAS*, 296, 367
- Cyburtt R. H. et al., 2010, *ApJS*, 189, 240
- Dale J. E., Ercolano B., Bonnell I. A., 2012, *MNRAS*, 424, 377
- Dale J. E., Ercolano B., Bonnell I. A., 2013, *MNRAS*, 430, 234
- de Jager C., Nieuwenhuijzen H., van der Hucht K. A., 1988, *A&AS*, 72, 259
- Decressin T., Mathis S., Palacios A., Siess L., Talon S., Charbonnel C., Zahn J.-P., 2009, *A&A*, 495, 271
- Deheuvels S. et al., 2010, *A&A*, 514, A31
- Dewitt H. E., Graboske H. C., Cooper M. S., 1973, *ApJ*, 181, 439
- Ekström S. et al., 2012, *A&A*, 537, A146
- Fagotto F., Bressan A., Bertelli G., Chiosi C., 1994, *A&AS*, 104, 365 (F94)
- Girardi L., Bressan A., Bertelli G., Chiosi C., 2000, *A&AS*, 141, 371
- Girardi L., Bertelli G., Bressan A., Chiosi C., Groenewegen M. A. T., Marigo P., Salasnich B., Weiss A., 2002, *A&A*, 391, 195
- Girardi L., Rubele S., Kerber L., 2009, *MNRAS*, 394, L74
- Graboske H. C., Dewitt H. E., Grossman A. S., Cooper M. S., 1973, *ApJ*, 181, 457
- Gräfener G., Hamann W.-R., 2008, *A&A*, 482, 945
- Gräfener G., Koesterke L., Hamann W.-R., 2002, *A&A*, 387, 244
- Grevesse N., Sauval A. J., 1998, *Space Sci. Rev.*, 85, 161 (GS98)
- Gustafsson B., Edvardsson B., Eriksson K., Jørgensen U. G., Nordlund Å., Plez B., 2008, *A&A*, 486, 951
- Haft M., Raffelt G., Weiss A., 1994, *ApJ*, 425, 222
- Hainich R. et al., 2014, *A&A*, 565, A27
- Hamann W.-R., Gräfener G., 2003, *A&A*, 410, 993
- Hamann W.-R., Gräfener G., 2004, *A&A*, 427, 697

- Hamann W.-R., Gräfener G., Liermann A., 2006, *A&A*, 457, 1015
 Hillier D. J., Miller D. L., 1998, *ApJ*, 496, 407
 Hollenbach D. J., Tielens A. G. G. M., 1999, *Rev. Mod. Phys.*, 71, 173
 Humphreys R. M., Davidson K., 1979, *ApJ*, 232, 409
 Iglesias C. A., Rogers F. J., 1996, *ApJ*, 464, 943
 Itoh N., Kohyama Y., 1983, *ApJ*, 275, 858
 Itoh N., Uchida S., Sakamoto Y., Kohyama Y., Nozawa S., 2008, *ApJ*, 677, 495
 Kamath D., Wood P. R., Soszyński I., Lebzelter T., 2010, *MNRAS*, 408, 522
 Kato S., 1966, *PASJ*, 18, 374
 Kennicutt R. C., Jr, 1998, *ARA&A*, 36, 189
 Kimm T., Cen R., 2014, *ApJ*, 788, 121
 Komatsu E. et al., 2011, *ApJS*, 192, 18
 Kudritzki R.-P., Puls J., 2000, *ARA&A*, 38, 613
 Kurucz R. L., 1993, in Dworetzky M. M., Castelli F., Faraggiana R., eds, *ASP Conf. Ser. Vol. 44, IAU Colloq. 138: Peculiar versus Normal Phenomena in A-type and Related Stars*. Astron. Soc. Pac., San Francisco, p. 87
 Lamers H. J. G. L. M., 1989, in Davidson K., Moffat A. F. J., Lamers H. J. G. L. M., eds, *Astrophysics and Space Science Library, Vol. 157, IAU Colloq. 113: Physics of Luminous Blue Variables*. Kluwer, Dordrecht, p. 135
 Ledoux P., 1947, *ApJ*, 105, 305
 Mackey J., Langer N., Mohamed S., Gvaramadze V. V., Neilson H. R., Meyer D. M.-A., 2014, *ASTRA Proceedings*, 1, 61
 Marigo P., Aringer B., 2009, *A&A*, 508, 1539
 Marigo P., Girardi L., Bressan A., Groenewegen M. A. T., Silva L., Granato G. L., 2008, *A&A*, 482, 883
 Martins F., Palacios A., 2013, *A&A*, 560, A16
 Meynet G., Maeder A., 2000, *A&A*, 361, 101
 Meynet G. et al., 2015, *A&A*, 575, A60
 Mokiem M. R. et al., 2007, *A&A*, 473, 603
 Muijres L. E., Vink J. S., de Koter A., Müller P. E., Langer N., 2012a, *A&A*, 537, A37
 Muijres L., Vink J. S., de Koter A., Hirschi R., Langer N., Yoon S.-C., 2012b, *A&A*, 546, A42
 Munakata H., Kohyama Y., Itoh N., 1985, *ApJ*, 296, 197
 Nanni A., Bressan A., Marigo P., Girardi L., 2013, *MNRAS*, 434, 2390
 Nanni A., Bressan A., Marigo P., Girardi L., 2014, *MNRAS*, 438, 2328
 Nugis T., Lamers H. J. G. L. M., 2000, *A&A*, 360, 227
 Pauldrach A., Puls J., Kudritzki R. P., 1986, *A&A*, 164, 86
 Paxton B., Bildsten L., Dotter A., Herwig F., Lesaffre P., Timmes F., 2011, *ApJS*, 192, 3
 Puls J., Springmann U., Lennon M., 2000, *A&AS*, 141, 23
 Salasnich B., Bressan A., Chiosi C., 1999, *A&A*, 342, 131
 Sander A., Hamann W.-R., Todt H., 2012, *A&A*, 540, A144
 Sarangi A., Cherchneff I., 2015, *A&A*, 575, A95
 Schaerer D., Hayes M., Verhamme A., Teyssier R., 2011, *A&A*, 531, A12
 Schmutz W., Hamann W.-R., Wessolowski U., 1989, *A&A*, 210, 236
 Schmutz W., Leitherer C., Gruenwald R., 1992, *PASP*, 104, 1164
 Schneider R., Ferrara A., Salvaterra R., 2004, *MNRAS*, 351, 1379
 Schwarzschild M., 1958, *Structure and Evolution of the Stars*. Princeton Univ. Press, Princeton, NJ
 Smith N., 2009, in Livio M., Villaver E., eds, *Space Telescope Science Institute Symp. Ser. 20, Massive Stars: From Pop III and GRBs to the Milky Way*. Cambridge Univ. Press, p. 187
 Smith N., 2014, *ARA&A*, 52, 487
 Smith L. F., Maeder A., 1991, *A&A*, 241, 77
 Smith N., Owocki S. P., 2006, *ApJ*, 645, L45
 Tang J., Bressan A., Rosenfield P., Slemmer A., Marigo P., Girardi L., Bianchi L., 2014, *MNRAS*, 445, 4287
 Torres G., Vaz L. P. R., Sandberg Lacy C. H., Claret A., 2014, *AJ*, 147, 36
 van Loon J. T., Cioni M.-R. L., Zijlstra A. A., Loup C., 2005, *A&A*, 438, 273
 Vink J. S., Gräfener G., 2012, *ApJ*, 751, L34
 Vink J. S., de Koter A., Lamers H. J. G. L. M., 2000, *A&A*, 362, 295
 Vink J. S., de Koter A., Lamers H. J. G. L. M., 2001, *A&A*, 369, 574
 Vink J. S., Muijres L. E., Anthonisse B., de Koter A., Gräfener G., Langer N., 2011, *A&A*, 531, A132
 Yu N., Wang J.-J., Li N., 2015, *MNRAS*, 446, 2566

This paper has been typeset from a $\text{\TeX}/\text{\LaTeX}$ file prepared by the author.